PERGAMON

International Journal of Heat and Mass Transfer 43 (2000) 945–962

International Journal of HEAT and MASS TRANSFER

www.elsevier.com/locate/ijhmt

The effect of hydrodynamic conditions on heat transfer in a complex viscoplastic flow field

Khaled J. Hammad*, [1]

Department of Mechanical, Aerospace, Industrial and Manufacturing Engineering, Polytechnic University, Rt. 110, Farmingdale, NY 11735, USA

Received 4 January 1999; received in revised form 18 May 1999

Abstract

The non-isothermal laminar flow of the Bingham non-Newtonian fluid through a sudden pipe expansion with a solid center-body placed upstream of the expansion plane, is investigated. The governing equations of conservation of mass, momentum and energy are solved using the finite-difference numerical technique. The effects of center-body-blockage-ratio, non-dimensional yield stress, Reynolds number, Prandtl number and Brinkman number on the flow and heat transfer characteristics are studied. The obtained results indicate the complex nature of the present viscoplastic flow and heat transfer problem and reveal new features not encountered in the case of Newtonian fluids.

Keywords: Non-Newtonian; Bingham plastic; Sudden expansion; Viscoplastic; Yield stress; Separated flows

1. Introduction

The Bingham constitutive equation has been extensively used to describe the rheology of numerous viscoplastic non-Newtonian fluids encountered in a large variety of industrial applications [1]. The general 3D constitutive equation relating the imposed stresses to the flow kinematics for a Bingham plastic is as follows [2]:

$$\tau_{ij}^* = \left(\eta_p + \frac{\tau_y}{\sqrt{\frac{1}{2}\dot{\gamma}_{II}^*}}\right)\dot{\gamma}_{ij}^* \quad \text{for } \tau_{II}^* > 2\tau_y^2 \tag{1a}$$

$$\dot{\gamma}_{ij}^* = 0 \quad \text{for } \tau_{II}^* \le 2\tau_y^2 \tag{1b}$$

Here η_p and Y are the plastic viscosity and yield stress (properties of the fluid), $\dot{\gamma}_{ij}^* = \partial u_i^*/\partial x_j^* + \partial u_j^*/\partial x_i^*$ is the rate-of-deformation tensor, and $\dot{\gamma}_{II}^*$ is the second invariant of the tensor $\dot{\gamma}_{ij}^*$, given by $\dot{\gamma}_{II}^* = \dot{\gamma}_{ij}^*\dot{\gamma}_{ij}^*$.

The apparent or effective viscosity displayed by a Bingham plastic is:

$$\mu_{eff}^*(\dot{\gamma}_{II}^*) = \eta_p + \frac{\tau_y}{\sqrt{\frac{1}{2}\dot{\gamma}_{II}^*}} \quad \text{for } \tau_{II}^* > 2\tau_y^2 \tag{2a}$$

$$\mu_{eff}^*(\dot{\gamma}_{II}^*) = \infty \quad \text{for } \tau_{II}^* \le 2\tau_y^2 \tag{2b}$$

In simple shear flows, rigid solid behavior is displayed as long as the imposed deviatoric stress tensor is less than or equal the materials yield stress. Shear stresses in excess of the yield value, however, lead to deformation rates and flow. Materials behaving in the

* Tel.: (201) 512-0037; fax: (201) 512-0120.

E-mail address: khaled.hammad@dantecmt.com (K.J. Hammad).

[1] Present address: Dantec Measurement Technology, 777 Corporate Drive, Mahwah, NJ 07430, USA.

0017-9310/00/$ - see front matter
PII: S0017-9310(99)00179-9

Nomenclature

Br	Brinkman number, $\eta_p u_b^2/\bar{k}(T_i - T_w)$
d, D	diameters of small and large pipes
ER	expansion ratio, D/d
$\bar{k}$	thermal conductivity of fluid
L_r	reattachment length
Nu	Nusselt number based on bulk temperature, $\frac{\partial\theta}{\partial r}\|_{R_w}/\theta_b$
Pr	Prandtl number, $\eta_p/\rho\alpha$
P	non-dimensional pressure, $P^*/\rho u_b^2$
r	non-dimensional radial distance, r^*/r_w
r_w, R_w	radii of small and large pipes
Re	Reynolds number, $\rho d u_b/\eta_p$
S	step height, $S = r_w$
T	temperature
u	non-dimensional streamwise velocity, u^*/u_b
u_b	streamwise bulk velocity, $2\pi\int_0^{r_w} u^* r^*\,dr^*/\pi r_w^2$
x	non-dimensional streamwise distance, x^*/S
Y	yield number, $\tau_y d/2\eta_p u_b$
α	thermal diffusivity
$\dot{\gamma}_{ij}$	rate of deformation tensor, $\partial u_i/\partial x_j + \partial u_j/\partial x_i$
$\dot{\gamma}_{II}$	second invariant of rate of deformation tensor, $\dot{\gamma}_{ij}\dot{\gamma}_{ij}$
η_p	plastic viscosity
κ	center-body-blockage-ratio
μ_{eff}	non-dimensional effective viscosity, $\mu_{eff} = \mu^*_{eff}/\eta_p$
θ	non-dimensional temperature, $(T - T_w)/(T_i - T_w)$
ρ	density
τ_{ij}	stress tensor element
τ_y	yield stress
ψ	non-dimensional stream function, $u = (1/r)(\partial\psi/\partial r), v = -(1/r)(\partial\psi/\partial x)$
ζ^-, ζ^+	non-dimensional lower and upper radial limits of the annular plug core

Subscripts

*	dimensional quantities
b	bulk properties
i, w	inlet and wall properties
min, max	minimum and maximum values

above-described manner include slurries, pastes, suspensions of solids in liquids, and emulsions. Industries in which viscoplastic behavior is encountered include those dealing with: composite materials, rubber, pharmaceuticals, biological fluids, plastics, petroleum, soap and detergents, cement, food products, paper pulp, paint, light and heavy chemicals, oil field operations, fermentation processes, plastic rocket propellants, electrorheological fluids, ore processing, and printing. Typical yield stress values can vary from less than a Pascal for blood [3] to tens of thousands of Pascals for plastic rocket propellants [4] and carbon black filled polymers [5].

The review paper by Bird et al. [1] provided a summary of known analytical solutions for the flow and heat transfer rates of Bingham plastics. All confined flows of Bingham plastics that were described in this review paper, however, were within simple geometries, i.e., those containing an unsheared plug whose boundaries are parallel to the physical boundaries. Heat transfer studies of Bingham plastics flowing in complex geometries in which the physical boundaries are not

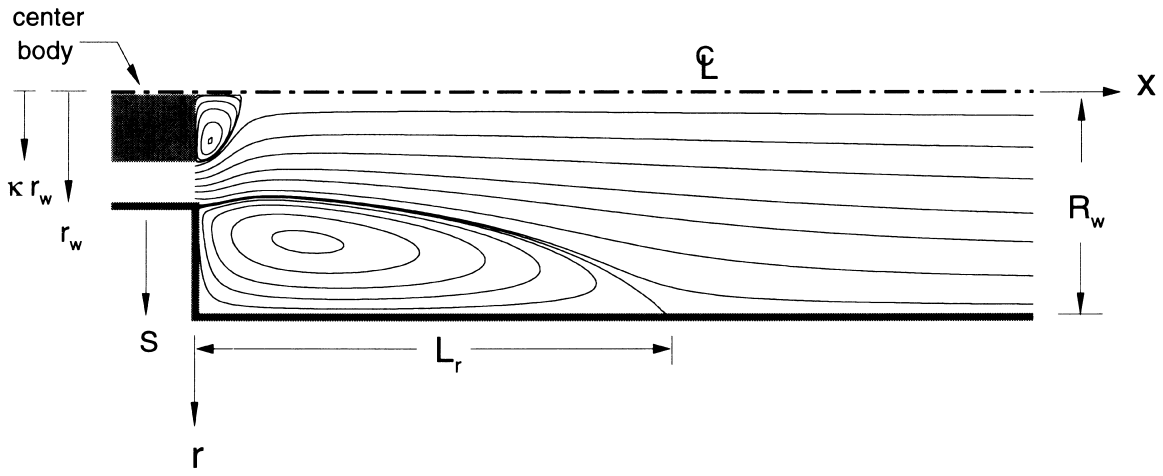

Fig. 1. Schematic diagram of flow geometry and coordinate system.

parallel are very limited. Additionally, most recent heat transfer studies of Bingham fluids, such as those by Vradis et al. [6] and Min et al. [7], focus on entrance pipe flows.

In summary, despite the considerable importance of Bingham fluids and their diverse applications, heat transfer studies related to complex and confined flows of such fluids have received little attention so far [8,9]. The present work, therefore, focuses on more complex non-isothermal confined flows of such non-Newtonian fluids. The selected flow geometry, shown in Fig. 1, is characterized by corner and central recirculation zones, when the fluid is Newtonian. Depending on the geometrical parameters, the fluid properties and the flow parameters, the flow downstream of the expansion plane may separate, re-attach and re-develop, thus forming corner and central recirculation zones. Using planar laser-sheet visualizations, Hammad et al. [10] demonstrated that separation, when a yield stress fluid suddenly expands, may or may not take place due to the possibility of forming a corner, ramp-like, non-moving zone. In addition, the impingement region of a separating yield stress fluid, was characterized by the existence of a non-deforming, attached to the wall, zone whose extent and location varied with the governing parameters.

Suddenly expanding internal flows are frequently encountered in engineering practice either by design, to promote mixing and enhance heat/mass transfer, or by default, such as devices commonly found in piping systems that are part of the fluid processing and transport. The unavoidable geometrical changes present in lines and processing equipment give rise to confined separated flow regions. Detailed understanding of the impact of geometrical changes encountered in practice on hydrodynamic conditions and the associated heat/mass transfer processes is, therefore, important. The geometrical simplicity and hydrodynamic complexity of the selected flow problem are the primary motives for selecting it to investigate the effects of the flow structure on heat transfer rates to the confining geometry in complex viscoplastic flow fields. The sudden expansion geometry is an ideal test geometry that is frequently encountered in practice. It has been used to shed light on the physics of wall-bounded separated and re-attached flows as well as the associated heat/mass transfer phenomenon [11–18]. A sudden expansion geometry has also been used to model flow and mass transfer in biological systems [19–23].

2. Governing equations

Based on the constitutive Eqs. (2a) and (2b), the non-dimensional form of the equations governing the incompressible, steady-state as well as constant properties flow of a Bingham fluid in an axisymmetric geometry is:

- Continuity

$$\frac{1}{r}\frac{\partial(rv)}{\partial r}+\frac{\partial u}{\partial x}=0 \tag{3}$$

- Equation of motion

  i. x-component

$$u\frac{\partial u}{\partial x}+v\frac{\partial u}{\partial r}=-\frac{\partial p}{\partial x}+\frac{1}{Re}\left\{\frac{\partial}{\partial x}\left(2\mu_{\text{eff}}\frac{\partial u}{\partial x}\right)+\frac{1}{r}\frac{\partial}{\partial r}\left(\mu_{\text{eff}}r\left(\frac{\partial v}{\partial x}+\frac{\partial u}{\partial r}\right)\right)\right\} \tag{4}$$

  ii. r-component

$$u\frac{\partial v}{\partial x}+v\frac{\partial v}{\partial r}=-\frac{\partial p}{\partial r}+\frac{1}{Re}\left\{\frac{1}{r}\frac{\partial}{\partial r}\left(2\mu_{\text{eff}}r\frac{\partial v}{\partial r}\right)+\frac{\partial}{\partial x}\left(\mu_{\text{eff}}\left(\frac{\partial v}{\partial x}+\frac{\partial u}{\partial r}\right)\right)-2\mu_{\text{eff}}\frac{v}{(r)^2}\right\} \tag{5}$$

- Equation of energy

$$u\frac{\partial\theta}{\partial x}+v\frac{\partial\theta}{\partial r}=\frac{1}{RePr}\left\{\frac{1}{r}\frac{\partial}{\partial r}\left(r\frac{\partial\theta}{\partial r}\right)+\frac{\partial}{\partial x}\left(\frac{\partial\theta}{\partial x}\right)\right\}+\frac{Br}{RePr}\mu_{\text{eff}}\left(\frac{1}{2}\dot{\gamma}_{\text{II}}\right) \tag{6}$$

Here, $\mu_{\text{eff}}=\mu^{*}_{\text{eff}}/\eta_{\text{p}}$ is the non-dimensional effective viscosity expressed as follows

$$\mu_{\text{eff}}(\dot{\gamma}_{\text{II}})=1+\frac{Y}{\sqrt{\frac{1}{2}\dot{\gamma}_{\text{II}}}}\quad\text{for }\tau_{\text{II}}>2\tau_y^2 \tag{7a}$$

$$\mu_{\text{eff}}(\dot{\gamma}_{\text{II}})=\infty\quad\text{for }\tau_{\text{II}}\le 2\tau_y^2 \tag{7b}$$

In cylindrical coordinates $\frac{1}{2}\dot{\gamma}_{\text{II}}$ is given by:

$$\frac{1}{2}\dot{\gamma}_{\text{II}}=2\left\{\left(\frac{\partial v}{\partial r}\right)^2+\left(\frac{v}{r}\right)^2+\left(\frac{\partial u}{\partial x}\right)^2\right\}+\left\{\frac{\partial v}{\partial x}+\frac{\partial u}{\partial r}\right\}^2 \tag{8}$$

Given a fixed axisymmetric geometry, the velocity, temperature and pressure fields obtained via numerically solving the above non-dimensionalized form of the governing equation, i.e., Eqs. (3)–(6), along with the Bingham constitutive Eqs. (7a) and (7b), are a function of Re, Pr, Br and Y. These non-dimensional numbers are defined as follows:

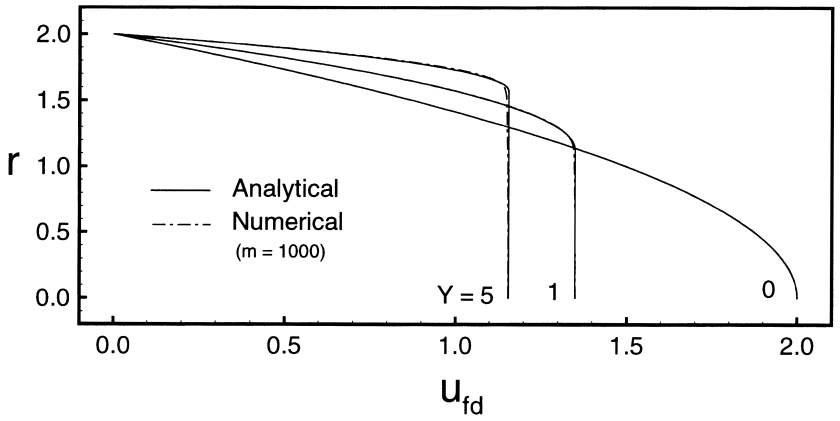

Fig. 2. Comparison of computed fully developed velocity profiles, in the downstream pipe when $m = 1000$, with the analytical ones for $Y = \{0,1,5\}$.

$$Y = \frac{\tau_y d}{2\eta_p u_b}, \quad Re = \frac{\rho d u_b}{\eta_p}, \quad Pr = \frac{\eta_p}{\rho\alpha} \text{ and } Br = \frac{\eta_p u_b^2}{\bar{k}(T_i - T_w)} \tag{9}$$

The other non-dimensional variables appearing in Eqs. (3)–(6) are:

$$x = \frac{x^*}{S}, \quad r = \frac{r^*}{S}, \quad u = \frac{u^*}{u_b}, \quad v = \frac{v^*}{u_b}, \quad p = \frac{p^*}{\rho u_b^2} \text{ and } \theta = \frac{T - T_w}{T_i - T_w} \tag{10}$$

The primary difficulty in obtaining numerical solution to complex flow problems (i.e., ones where the boundaries of the confining geometry are not parallel), of viscoplastic fluids is the existence of a surface separating the regions of sheared fluid from those of non-sheared fluid. Utilizing the previously described effective viscosity formulation eliminates the need to track the surface separating these two flow regions and simplifies the solution. It leads, however, to singularities since the effective viscosity μ_{eff} attains an infinite value in regions where $\dot{\gamma}_{ij} = 0$, such as core regions of the flow. In order to avoid such a problem, Eqs. (7a) and (7b) are replaced by the following constitutive equation, a similar dimensional form of which was originally proposed by Papanastasiou [24]:

$$\mu_{\text{eff}}(\dot{\gamma}_{II}) = 1 + \frac{Y}{\sqrt{\frac{1}{2}\dot{\gamma}_{II}}}\left(1 - e^{-m\sqrt{\frac{1}{2}\dot{\gamma}_{II}}}\right) \tag{11}$$

Here, m is an exponential growth parameter. This approach has been utilized and proved to provide a good approximation of a Bingham fluid rheology at both the low and high ends of the shear rate spectrum, see Ellwood et al. [25]. Extensive numerical experimentation led to the establishment of $m = 1000$ as high enough to obtain accurate solutions. This is further verified via comparing analytical axial velocity profiles corresponding to fully developed flow conditions in the downstream pipe to those computed at $m = 1000$. As Fig. 2 shows, the agreement between analytical and computed results is excellent.

3. Method of solution

The governing partial differential Eqs. (3)–(7b) are solved numerically utilizing a finite-difference scheme. This solution technique has been tested and proved to be highly accurate and computationally efficient for solving non-Newtonian convective heat transfer problems [16,26]. Fully second order accurate finite-difference approximations are used for the derivatives appearing in the governing equations. Centered differences are used in all cases with the exception of the convective streamwise derivatives, which are upwinded, using first order approximations. Further details regarding the finite-difference form of the governing partial differential equations along with the solution methodology can be found in either in [26] or [16], and, therefore, will not be repeated here.

The boundary conditions selected for the present flow and heat transfer problem are:

At inlet $u = u(r), \quad v = 0, \quad \theta = 1$

At vertical wall and solid center-body $u = 0, \quad v = 0,$

$\theta = 1$

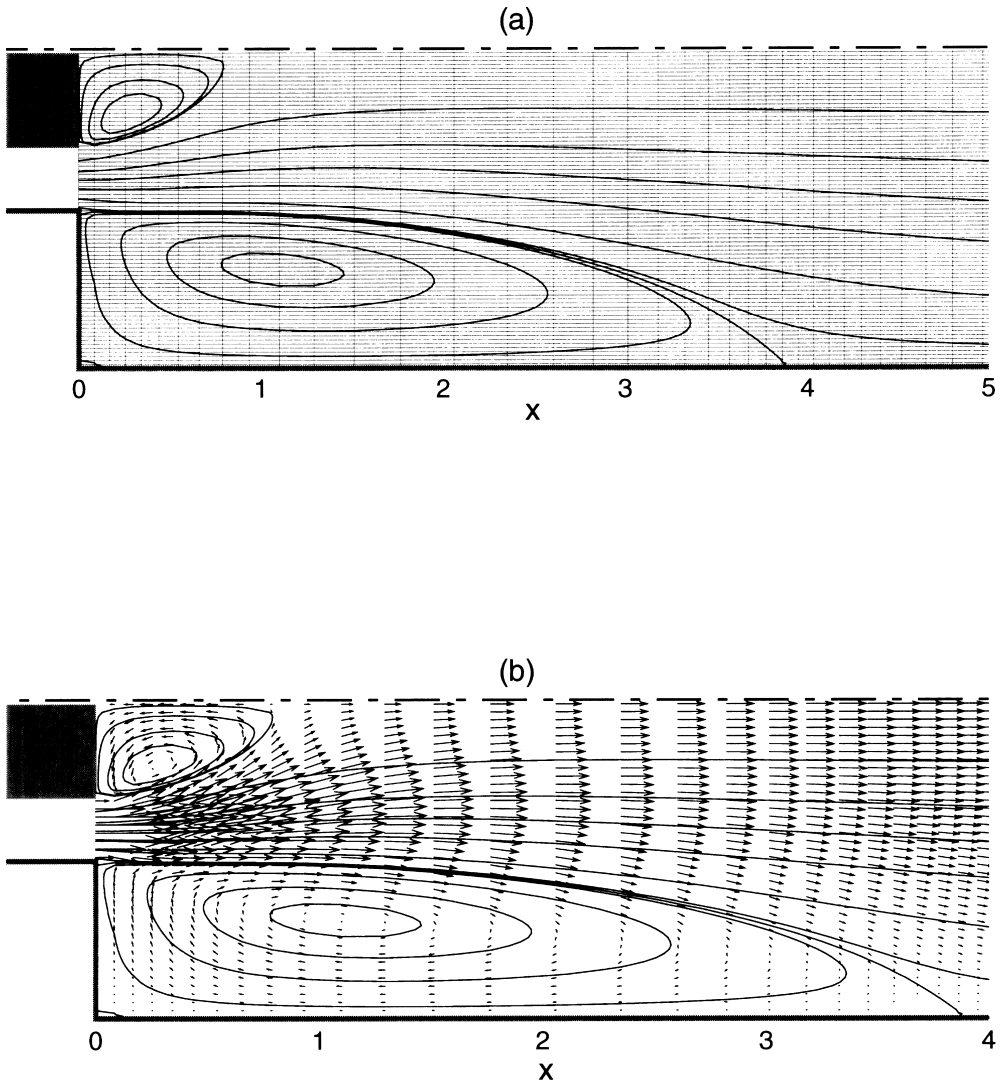

Fig. 3. (a) Computational grid superposed on streamlines; (b) velocity field superposed on streamlines. Both are for $Y = 0$, $Re = 100$ and $\kappa = 0.6$.

At downstream horizontal wall $u = 0, \quad v = 0, \quad \theta = 0$

Along the centerline $v = \dfrac{\partial u}{\partial r} = \dfrac{\partial p}{\partial r} = \dfrac{\partial \theta}{\partial r} = 0$

At outlet $v = p = \dfrac{\partial u}{\partial x} = \dfrac{\partial(\theta/\theta_b)}{\partial x} = 0$

The outlet boundary conditions were applied sufficiently far downstream the plane of expansion to ensure that the computed results were independent of the location of application of these boundary conditions. All computations employed a 150×80 grid. As shown in Fig. 3, a small and uniform vertical grid spacing was used while the horizontal ones were variable and adjusted such that, grid clustering was achieved in the vicinity of the expansion plane and point of reattachment. Fig. 3 also contains an overview of the velocity vector distribution superposed on the flow field streamlines. Extensive numerical experimentation established the grid-independent nature of the results obtained using the above-defined grid (e.g. A 200×100 grid resulted in flow field characteristics, such as reattachment lengths, L_r, and axial distributions of wall heat transfer rates that were identical to the ones obtained using the 150×80 grid). Further, some of the presently computed results are compared to an experimental set of data obtained by Hammad et al. [18] and the flow visualization results of Macagno and Hung [11]. The comparison, shown in Fig. 4, dis-

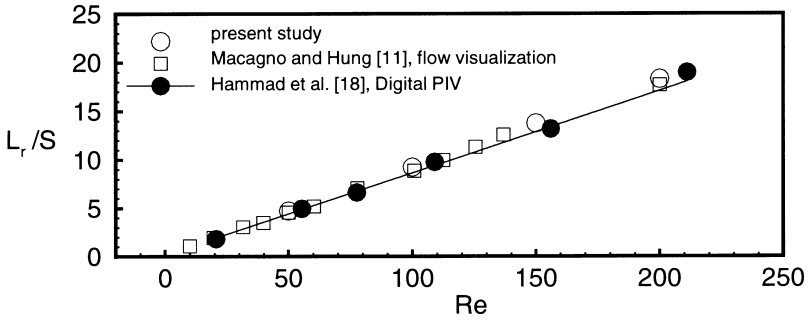

Fig. 4. Reattachment length variation with Reynolds number for $Y = 0$ and $\kappa = 0$. A comparison between computed and available experimental data.

plays the effect of the Reynolds number on the length of reattachment, L_r, for a Newtonian fluid in the absence of a center-body. It can be seen that the reattachment length increases linearly with the Reynolds number. In addition, a very favorable agreement is obtained between the present numerical predictions and the experimental results.

The axial velocity profile between the solid centerbody and the confining upstream pipe, i.e., prior to the expansion plane, is identical to that of a fully developed annular flow of a Bingham fluid. As shown in Fig. 5 this annular flow is characterized by the existence of two liquid regions in the vicinity of both the solid center-body and outer pipe. The first liquid region lies within κ and ζ^-, while the second is bounded by ζ^+ and 1. A core plug zone having a radial extent of $\zeta^+ - \zeta^-$ separates these two liquid regions. For a Newtonian fluid, i.e., $Y = 0$, $\zeta^+ - \zeta^- = 0$. The magnitude of $\zeta^+ - \zeta^-$, however, increases with Y and asymptotically approaches $1 - \kappa$, as $Y \to \infty$. The dimensional form of the fully developed axial velocity profile of a Bingham plastic between two con-

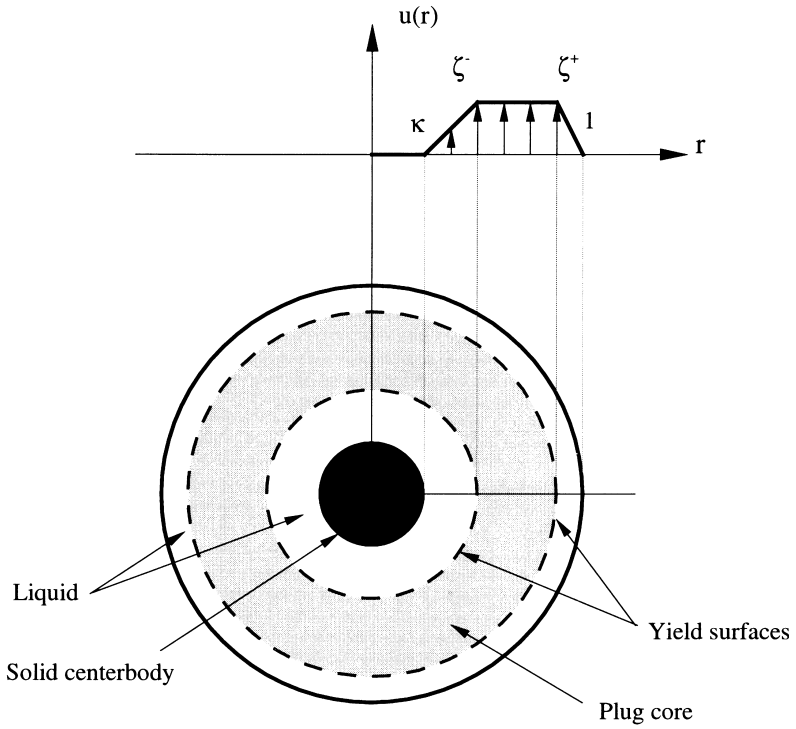

Fig. 5. Schematic diagram of a viscoplastic flow field between two concentric pipes.

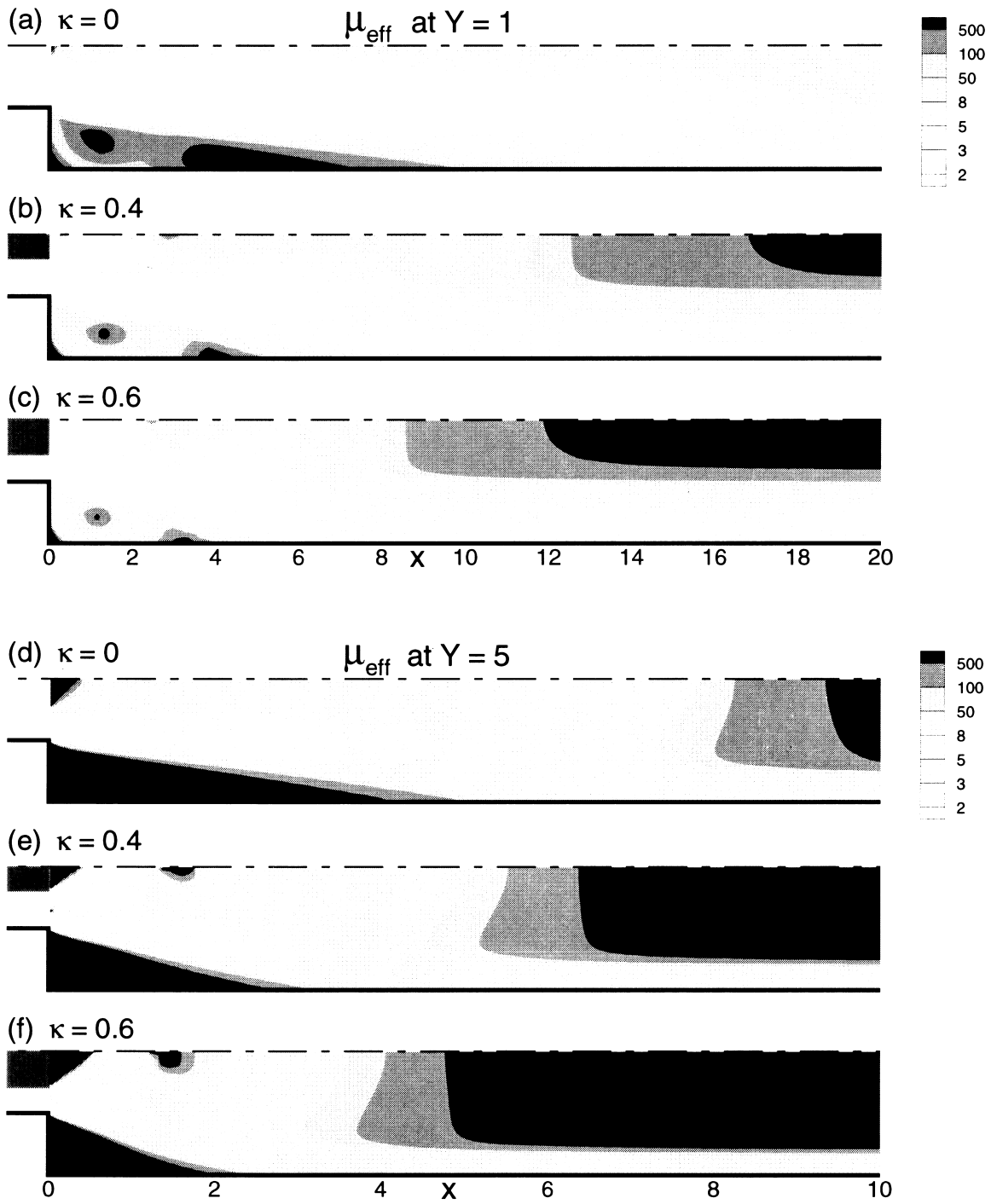

Fig. 6. Influence of center-body-blockage-ratio on non-dimensional effective viscosity fields for $Re = 200$ and $Y = \{1,5\}$.

centric pipes can be found in [1]. The corresponding non-dimensional form of the velocity profile, based on the variables used here, is given below:

$$u(r) = \frac{1-\kappa^2}{\xi}\int_{\kappa}^{r} r^{-1}\left(\zeta^+\zeta^- - r^2 - \left(\zeta^+ - \zeta^-\right)\right)\mathrm{d}r \quad \text{for } \kappa \le r \le \zeta^- \tag{12a}$$

$$u(r) = u_{\max} = u(\zeta^-) = u(\zeta^+) \quad \text{for } \zeta^- \le r \le \zeta^+ \tag{12b}$$

$$u(r) = \frac{1-\kappa^2}{\xi}\int_{r}^{1} r^{-1}\left(r^2 - \left(\zeta^+ - \zeta^-\right) - \zeta^+\zeta^-\right)\mathrm{d}r \quad \text{for } \zeta^+ \le r \le 1 \tag{12c}$$

where

$$\xi = \int_{\kappa}^{\zeta^-} r\left(r^2 + \left(\zeta^+ - \zeta^-\right) - \zeta^+\zeta^-\right)\mathrm{d}r - \int_{\zeta^+}^{1} r\left(\zeta^+\zeta^- - r^2 + \left(\zeta^+ - \zeta^-\right)\right)\mathrm{d}r$$

Here, ζ^- and ζ^+ are obtained from the condition $u(\zeta^-) = u(\zeta^+)$, which requires solving for the roots of the following equations:

$$\int_{\kappa}^{\zeta^-} r^{-1}\left(\zeta^+\zeta^- - r^2 - \left(\zeta^+ - \zeta^-\right)\right)\mathrm{d}r - \int_{\zeta^+}^{1} r^{-1}\left(r^2 - \left(\zeta^+ - \zeta^-\right) - \zeta^+\zeta^-\right)\mathrm{d}r = 0 \tag{13}$$

$$\frac{(1-\kappa^2)\left(\zeta^+ - \zeta^-\right)}{Y} - \int_{\kappa}^{\zeta^-} r\left(r^2 - \left(\zeta^+ - \zeta^-\right) - \zeta^+\zeta^-\right)\mathrm{d}r - \int_{\zeta^+}^{1} r\left(r^2 - \left(\zeta^+ - \zeta^-\right) - \zeta^+\zeta^-\right)\mathrm{d}r = 0 \tag{14}$$

4. Results and discussion

Heat transfer rates from the laminar viscoplastic flow field within the geometry depicted in Fig. 1 to the surrounding walls are influenced by the expansion ratio (ER); the Reynolds (Re), yield (Y), Prandtl (Pr), and Brinkman (Br) numbers; and the blockage ratio (κ). The heat transfer results to be presented are obtained from a systematic parametric study in which, these governing parameters were assigned the following values: $ER = \{2\}$; $Re = \{100,200,400\}$; $Y = \{0,1,5\}$; $Pr = \{1,7,15\}$; $Br = \{0,1,2\}$; $\kappa = \{0,0.4,0.6\}$. All fluid properties are assumed to be temperature and pressure independent throughout this study.

4.1. Effective viscosity fields

The complexity of the flow patterns existing inside the present geometry is best illustrated via inspecting the non-dimensional effective viscosity (μ_{eff}) distributions shown in Fig. 6 for $Re = 200$ and $\kappa = \{0,0.4,0.6\}$. Fig. 6(a)–(c) correspond to $Y = 1$, while Fig. 6(d)–(f) correspond to $Y = 5$. When the centerbody is absent, as shown in Fig. 6(a) and (d), the confined flow structure is typically characterized by a plug zone existing around the centerline in the upstream pipe that vanishes, once the plane of expansion is passed. The destruction of the plug zone is followed by high rates of deformation region along the centerline. The onset of formation of another plug zone, at a certain downstream location, indicates a downstream flow field redevelopment. Complete development of the downstream plug zone implies that fully developed conditions have been established. Flow field redevelopment downstream of the expansion plane becomes more rapid when the yield number is increased from 1 to 5, as noticed from the earlier appearance of the plug zone in the downstream pipe, Fig. 6(a) and (d). These observations are in agreement with those of Scott and Mirza [27], and Vradis and Ötügen [28]. Both have numerically studied axisymmetric sudden expansion flows of a Bingham plastic and established the rapid reduction in flow redevelopment and reattachment lengths when increasing a non-dimensionalized yield stress.

At a fixed Reynolds number and for a given geometry, i.e., fixed ER and κ, the formation of a corner vortex depends on the yield number value. For low yield numbers, Fig. 6(a), a corner vortex forms. For high yield numbers, a substantial non-moving, ramp-like, corner zone replaces the corner vortex, as clearly evidenced from the large corner values of μ_{eff} shown in Fig. 6(d). In general, a corner vortex exists for a combination of high Reynolds and low yield numbers. Also, for yield stress fluids, a non-deforming, attached to the wall, impingement zone and another very small, stagnant, corner zone accompany the formation of the corner vortex, as clearly shown in Fig. 6(a). Accurate, digital particle image velocimetry measurements [29] and planar, laser-sheet visualizations [10] support these conclusions related to transitions in the observed flow patterns. These important flow pattern transitions were first observed, experimentally, by Hammad et al. [10] and have not been reported in any similar previous study, including the numerical studies by Scott and Mirza [27], Vradis and Hammad [8] and Vradis and Ötügen [28].

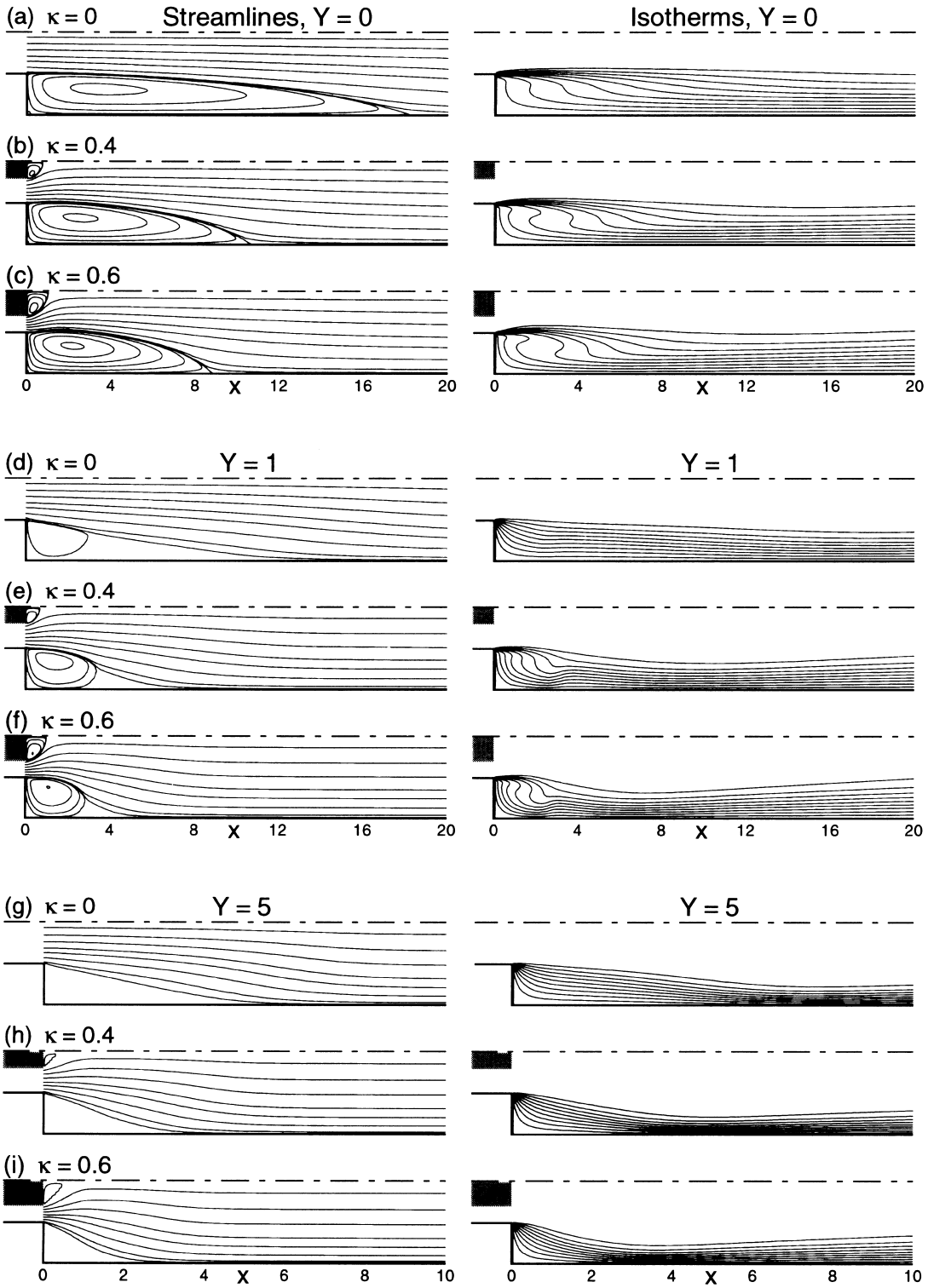

Fig. 7. Streamlines and Isotherms variation with center-body-blockage-ratio, for $Re = 200$, $Pr = 7$, $Br = 0$ and $Y = \{0,1,5\}$.

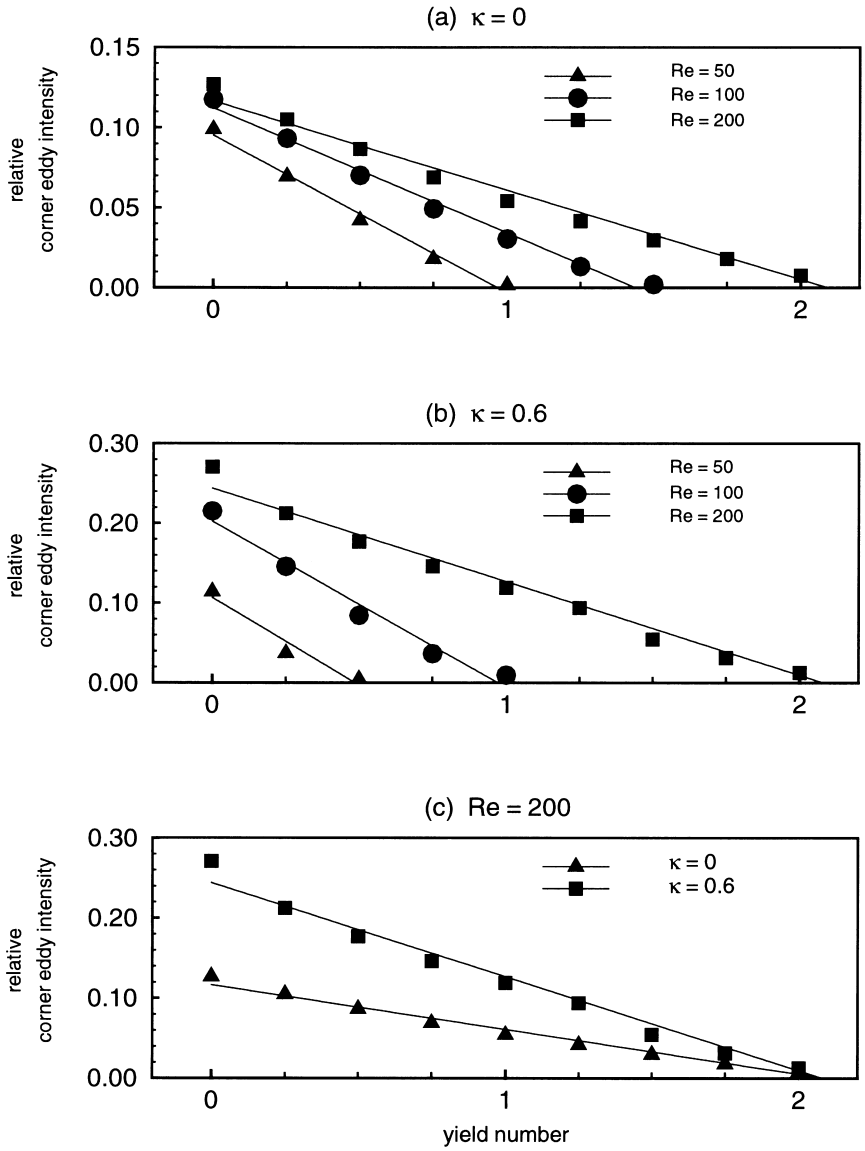

Fig. 8. Relative corner eddy intensity versus yield number for $Re = \{50,100,200\}$ and $\kappa = \{0,0.6\}$.

The placement of a solid center-body upstream of the expansion, shortens the redevelopment length and reduces the extent of both the corner and the impingement flow regions, Fig. 6(a)–(f). These changes can be attributed to both, more effective momentum diffusion mechanisms towards the surrounding walls and the central counter-rotating pair of vortexes. The center of each vortex existing in the flow field generally possesses a μ_{eff} value that is distinctly higher than those around it. On the other hand, the overall μ_{eff} distribution within a vortex depends on the recirculation intensity. For example, the corner vortex appearing in Fig. 6(a) is weaker in comparison to the ones shown in Fig. 6(b)–(c), and is characterized, therefore, by higher overall μ_{eff} values.

4.2. Streamlines and isotherms

The streamline contour plots shown in Fig. 7 demonstrate the effect of the center-body-blockage-ratio, $\kappa = \{0,0.4,0.6\}$, on the flow field for $Y = \{0,1,5\}$. To illustrate the impact of the flow structure on the thermal field characteristics, the isotherms $\theta = \{0.1,0.2,0.3,0.4,0.5,0.6,0.7,0.8,0.8,0.9\}$ corresponding to $Pr = 7$ and $Br = 0$, are also displayed in Fig. 7. The $\theta = 0.1$ isotherms are close to the walls, while those of

$\theta = 0.9$ are close to the centerline. The Reynolds number for all cases shown in Fig. 7 was fixed at 200. For the Newtonian fluid case, Fig. 7(a)–(c), the corner flow region consists of a substantial corner vortex. For $Y = 1$, the corner vortexes formed are smaller and weaker in comparison to those corresponding to $Y = 0$. For $Y = 5$, the streamlines shown in Fig. 7(g)–(i) display a substantial, stagnant, corner zone, as opposed to the corner vortex obtained for the yield numbers 0 and 1. For yield stress fluids, a non-moving impingement zone, as shown in Fig. 7(d)–(f), bound the corner flow region. The case corresponding to $\kappa = 0$, Fig. 7(d), captures what happens immediately after the onset of deformation in the corner region, as evidenced from the formation of a weak corner vortex, large impingement zone and a small corner dead zone.

The placement of the center-body leads to the following:

1. the creation of a central vortex whose size and intensity increase with κ;
2. strengthens the corner vortex and reduces its axial extent as shown in Fig. 7(a)–(f), for $Y = 0$ and 1;
3. shortens the redevelopment length as shown in Fig. 7(a)–(i), for $Y = 0$, 1 and 5; and
4. smaller impingement and stagnant corner zones as shown in Fig. 7(d)–(f) and (g)–(i), respectively.

The impact of center-body placement on the thermal field include: (1) increased distortions of the isotherms in the vicinity of the corner as can be seen from the temperature distributions corresponding to $Y = 0$ and 1; and (2) more pronounced, local, compressions in the thermal boundary layer by either the corner vortex or the incoming wall bound flow. The first effect is attributed to the rise in corner recirculation intensity with κ, and seems to be restricted to the corner vortex domain. Also, increasing the intensity of the corner vortex at a constant Pr, leads to isotherms having a shape that is closer to that of the flow streamlines. The second effect steepens temperature gradients and is expected to increase wall heat transfer rates. The local compressions in the thermal boundary layer appearing in the corner vortex region and downstream of the impingement region are most clearly seen in the isotherm plots shown in Fig. 7(e) and (f). The non-deforming, attached to the wall region, appearing in Fig. 7(d)–(f), gives rise to a diffusion limited heat transfer zone that is characterized by, for $Pr > 1$, a thicker thermal boundary layer than those displayed further upstream or downstream. Diffusion limited heat transfer zones are associated with vanishing rates of deformation regions existing throughout the flow field of yield stress fluids such as moving plug zones, characterized by zero velocity-gradients (typically found close to the centerline), or finite-size non-moving zones (attached to the wall such as impingement and corner zones).

4.3. Corner eddy intensity

For a given geometry, i.e., fixed ER and κ, the formation of a corner eddy or vortex depends on the values of both Re and Y. For every Reynolds number, there is a corresponding critical yield number ($Y_{cr} \equiv Y_{cr}(Re)$). A corner eddy exists whenever $Y < Y_{cr}$, as was shown earlier in Fig. 7(a)–(f). Also, for yield stress fluids, a non-moving wall impingement zone and another very small dead corner zone accompany the formation of a corner eddy. If $Y > Y_{cr}$, then only a substantial corner dead zone exists, as was shown in Fig. 7(f)–(i). The variation of the critical yields number with both, the Reynolds number and κ is illustrated in Fig. 8. Fig. 8 is a plot of the relative corner eddy intensity against the yield number, for $Re = \{50,100,200\}$, as shown in Fig. 8(a) and 6(b), when the center-body-blockage-ratio is 0 and 0.6, respectively. The relative corner eddy intensity (RCEI) is defined as the maximum amount of back flow in the vortex region relative to the inlet flow rate or $-\psi_{min}/\psi_{max}$. Fig. 8(c) compares the variation of RCEI with the yield number at $\kappa = 0$ to that of $\kappa = 0.6$, when the Reynolds number is fixed at 200. Fig. 8 demonstrates the strong dependency of RCEI on the yield number, the Reynolds number and the center-body-blockage-ratio, which decreases with Y, while increasing with both Re and κ. For zero yield stress fluids, the dependence of RCEI on the Reynolds number weakens at high Reynolds numbers, hinting at the existence of an asymptotic limit. For $Re \leq 200$ and $\kappa \leq 0.6$, as shown in Fig. 8(a) and (b), a yield number of 2.25 is more than sufficient to bring the corner vortex to a total halt, and thus creating a substantial corner dead-zone. Increasing the yield number and reducing the Reynolds number would always lead to a reduction in the eddy intensity. This is expected since larger yield numbers increase the viscosity values throughout the eddy region, thus lowering rates of deformation and, hence, recirculation intensity. Also, at fixed Y and κ values, increasing Re lead to increased momentum transfer into the corner region and thus intensifies the recirculation. The monotonic and rather significant decrease of RCEI with the yield number at either a constant Reynolds number or a constant κ is rather linear, as clearly shown in Fig. 8(a)–(c). Therefore, a linear regression fit was used to extract critical yield numbers corresponding to all cases shown in Fig. 8. The critical yield number is Y, at which RCEI becomes zero. For $\kappa = 0$, the Y_{cr} values were 0.96, 1.43 and 2.07, when the Reynolds numbers were 50, 100 and 200, respectively. However, for $\kappa = 0.6$, the Y_{cr} values were 0.48, 0.961 and 2.06.

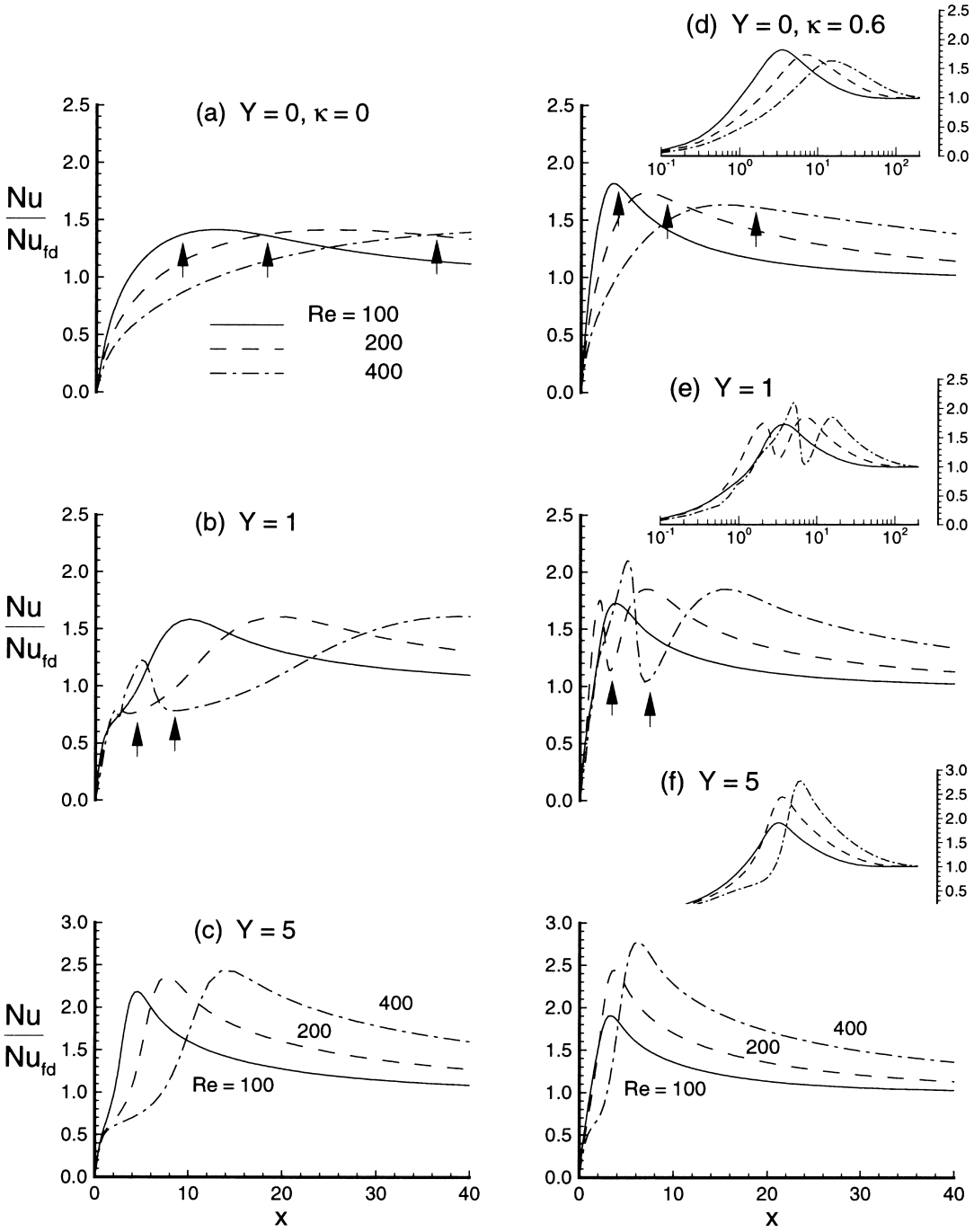

Fig. 9. Influence of Reynolds number on wall heat transfer distributions for $Pr = 7$ and $Br = 0$.

4.4. Wall heat transfer rates

Transitions in the flow patterns within the present geometry, influence heat transfer from the viscoplastic fluid to the surrounding walls. To illustrate these influences, the computed Nusselt numbers (Nu) are normalized with the fully developed ones prevailing far downstream of the expansion (Nu_{fd}), and used to present Nu/Nu_{fd} vs. x. In the present study, Nu_{fd} depends on κ, Y and Br. To better elucidate the impact of local

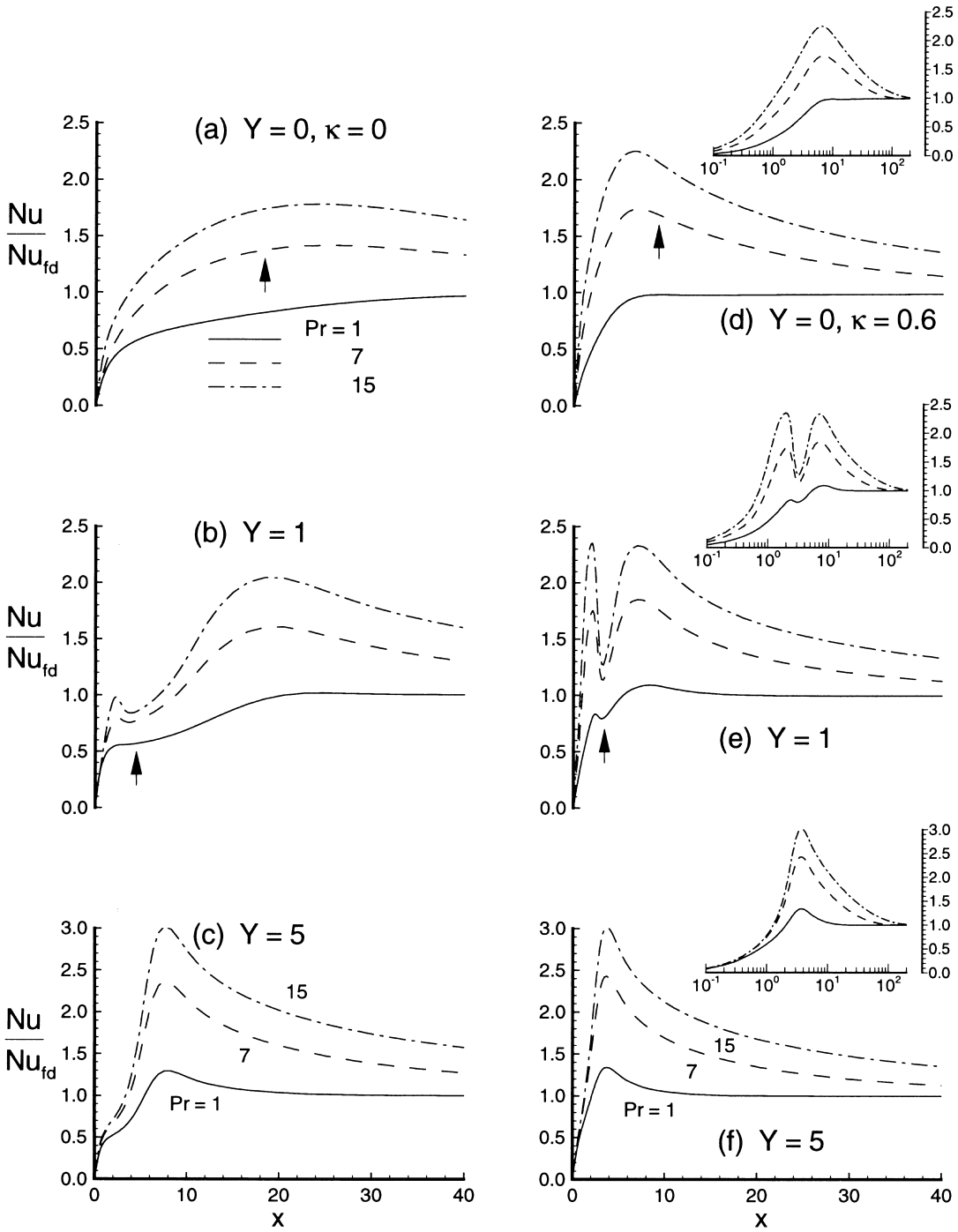

Fig. 10. Influence of Prandtl number on wall heat transfer distributions for $Re = 200$ and $Br = 0$.

hydrodynamic conditions, zero wall shear stress locations, i.e., x at $\tau_w = 0$, are highlighted by the presence of solid arrows. Each zero wall shear stress point marks the axial extent of the corner flow region, which is bounded by either the reattachment point (Newtonian fluid) or the center of the impingement region center (separated viscoplastic flow field, e.g. $Y = 1$ and $Re = 200$). A special emphasis is paid to the

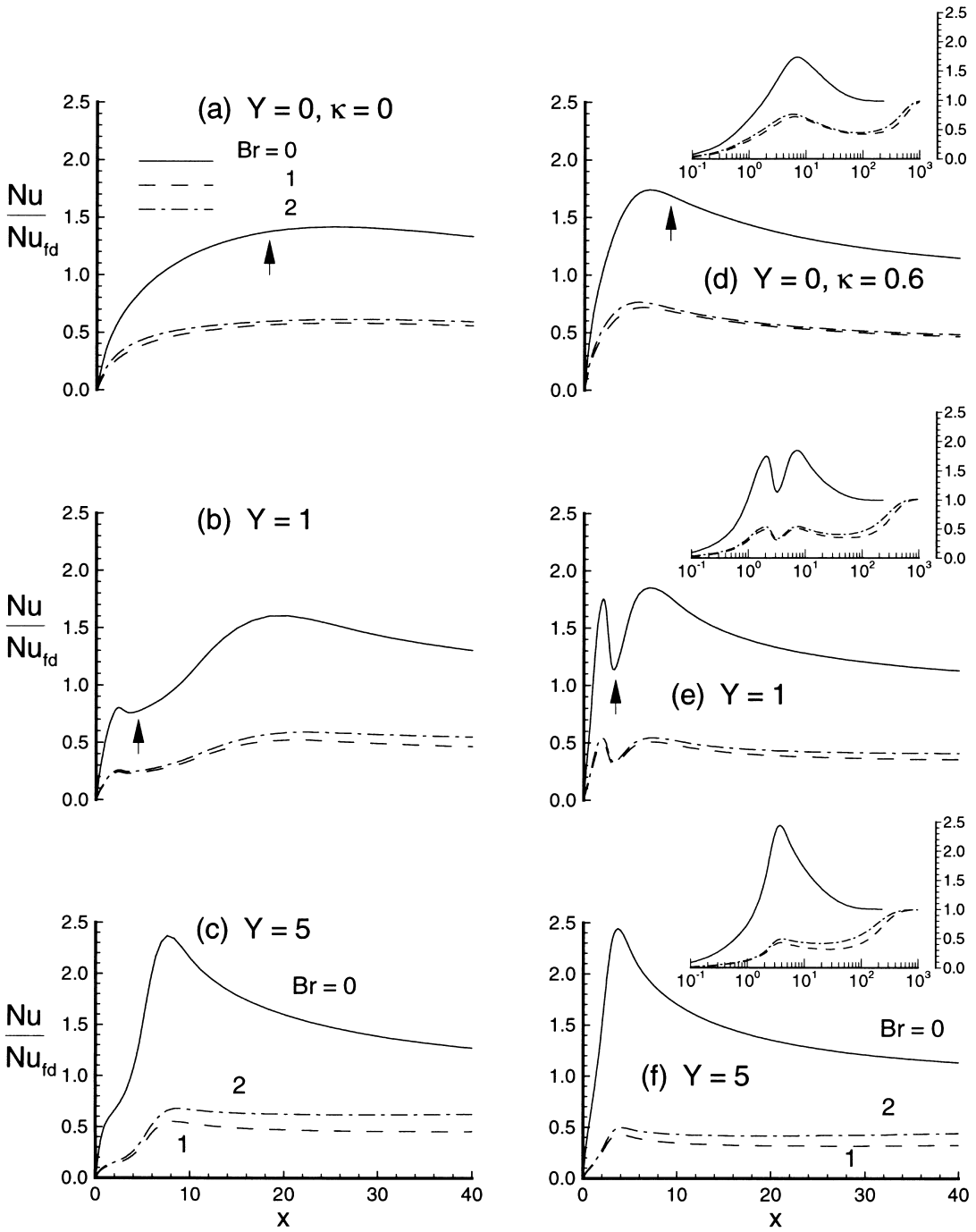

Fig. 11. Influence of viscous heating on wall heat transfer distributions for $Re = 200$, and $Pr = 7$.

relative location of all peak heat transfer points to that of $\tau_w = 0$ and how both are affected by the governing parameters.

4.4.1. Reynolds number effect

Influence of Reynolds number on heat transfer distributions along the downstream pipe are demonstrated in Fig. 9 for $Re = \{100,200,400\}$, $Y = \{0,1,5\}$ and $\kappa = \{0,0.6\}$. The Prandtl and Brinkman numbers are fixed at 7 and 0, respectively. The shown arrows, mark the axial locations of the reattachment point (Fig. 9(a) and (d)) and the center of impingement

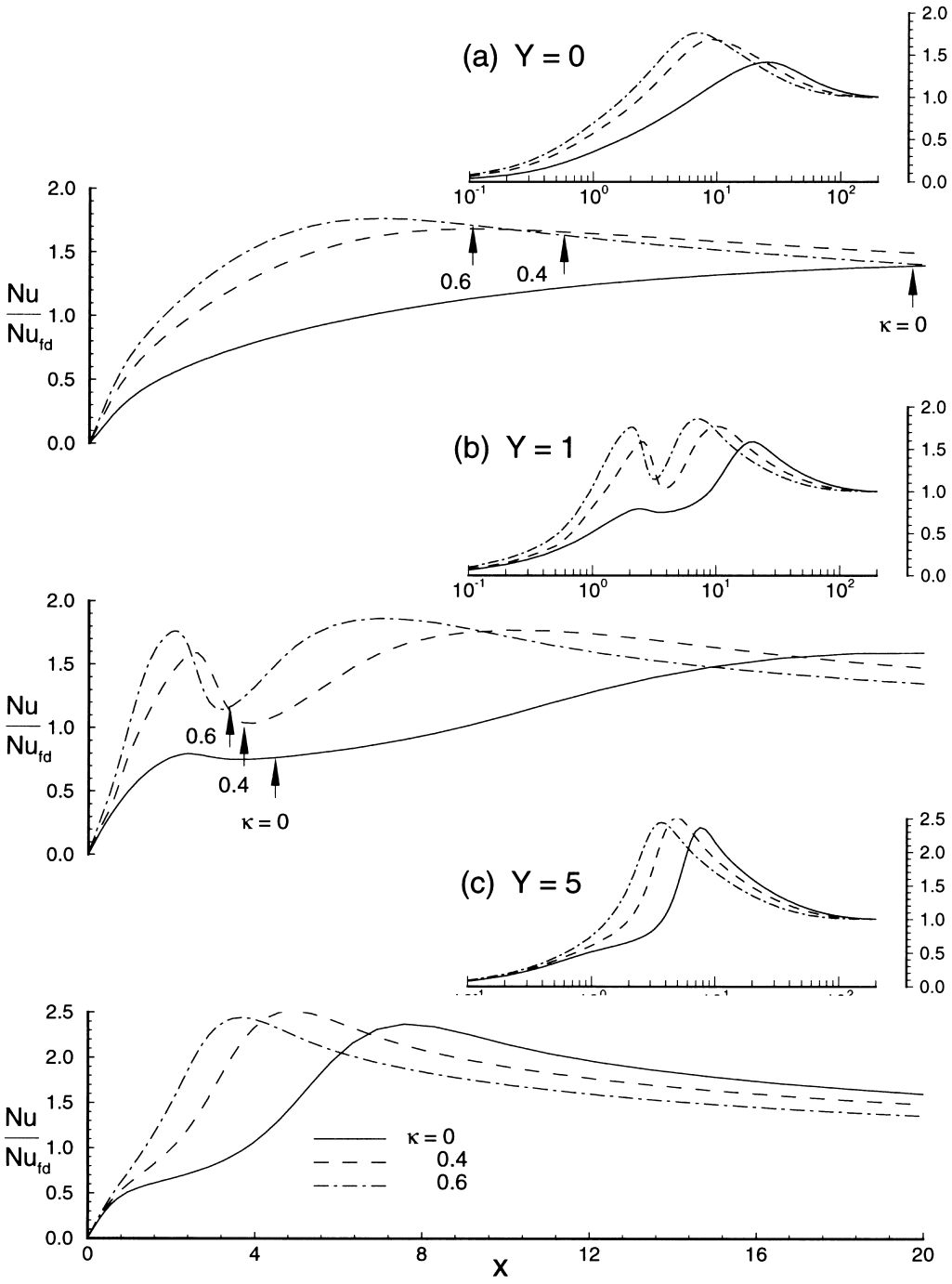

Fig. 12. Influence of center-body-blockage-ratio on wall heat transfer distributions for $Re = 200$, $Pr = 7$, and $Br = 0$.

region ($Re = 200$ and 400 in Fig. 9(b) and (e)). Cases corresponding to $Re = 100$ in Fig. 9(b) and (e) as well as all those shown in Fig. 9(c) and (f) result in a non-moving corner zone. As shown, all arrows move downstream with the Reynolds number, which, in turn, leads to a similar movement in the maximum heat transfer points, i.e., further downstream. Additionally, increasing the Reynolds number can lead to the mobilization of the corner non-moving zone and the creation of a corner recirculation region and another stagnant impingement region, as shown in Fig. 9(b) and (e). As shown in Fig. 9, Nu/Nu_{fd} profiles characterized by a

single peak value are associated with either Newtonian or non-separating viscoplastic flow patterns. The appearance of two peak Nu/Nu_{fd} values, is only possible for a separating, i.e., corner vortex forming, viscoplastic flow pattern. These two peak values are located close to the corner vortex center and downstream of the impingement region. For a Prandtl number of 7, the appearance of the two peak points indicates that convection plays a more important heat transfer role, within these two flow regions, compared to that of molecular diffusion. However, diffusion heat transfer dominates throughout all vanishing rates of deformation regions, such as the impingement flow region corresponding to $Y = 1$, which, for $Pr > 1$, result in a sudden drop in the heat transfer rates to the confining walls, as clearly seen in Fig. 9(b) and (e).

4.4.2. The effect of Prandtl number

The impact of Prandtl number on heat transfer distributions along the downstream pipe are illustrated in Fig. 10 for $Pr = \{1,7,15\}$, $Y = \{0,1,5\}$ and $\kappa = \{0,0.6\}$. The Reynolds and Brinkman numbers are fixed at 200 and 0, respectively. For $Re = 200$, the critical yield numbers are 2.07 and 2.06 when $\kappa = 0$ and 0.6, respectively. Therefore, all curves shown in Fig. 10(b) and (e), for $Y = 1$, correspond to a separating viscoplastic flow field, while those of Fig. 10(c) and (f), for $Y = 5$, are associated with a non-separating viscoplastic flow field. The arrows appearing in Fig. 10(a) and (d) indicate the position of the reattachment point, while those of Fig. 10(b) and (e) mark the axial position of the center of the impingement region.

The early comments regarding how transitions in the flow pattern affect the overall wall heat transfer characteristics remain valid for $Pr = 1$, 7 and 15. However, for $Y = 0$ and $Pr = 1$, Nu/Nu_{fd} increases monotically with x, as shown in Fig. 10(a) and (d). Whenever applicable, the heat transfer augmentation close to both the corner vortex center and/or downstream of the impingement region is more dramatic for larger Prandtl numbers. The highest wall heat transfer augmentation, i.e., $Nu/Nu_{fd} \cong 3$, corresponds to $Y = 5$, $Pr = 15$ and $\kappa = 0.6$.

4.4.3. The effect of viscous heating

Viscous heating effects on the amount of heat transferred to the downstream wall are investigated by varying the Brinkman number as shown in Fig. 11 for $Br = \{0,1,2\}$ $Y = \{0,1,5\}$ and $\kappa = \{0,0.6\}$. The Reynolds and Prandtl numbers are fixed at 200 and 7, respectively. As shown, heat transfer enhancement, i.e., $Nu/Nu_{fd} > 1$, does not appear for $Br = 1$ and 2. For $Br > 0$, or whenever viscous heating is incorporated, increasing Br results in higher overall Nu/Nu_{fd} distributions. It should be emphasized that, for fixed Y and κ values, $Nu_{fd}|_{Br>0}$ here is much larger than $Nu_{fd}|_{Br=0}$, which accounts for the large discrepancy between $Nu_{fd}|_{Br=0}$ and $Nu/Nu_{fd}|_{Br>0}$ profiles shown in Fig. 11. For example, at $Y = 0$ and $\kappa = 0$, $Nu_{fd}|_{Br=0} \cong 0.92$ and $Nu_{fd}|_{Br>0} \cong 2.4$. For $Y = 5$ and $\kappa = 0$, $Nu_{fd}|_{Br=0} \cong 1.26$ and $Nu_{fd}|_{Br>0} \cong 7.4$. A detailed treatment of viscous heating effects on Nu_{fd} can be found in Payvar [30].

4.4.4. The effect of center-body-blockage-ratio

Variations in wall heat transfer distributions with center-body-blockage-ratio are shown in Fig. 12 for $\kappa = \{0,0.4,0.6\}$ and $Y = \{0,1,5\}$. The Reynolds, Prandtl and Brinkman numbers are fixed at 200, 7 and 0, respectively. All arrows appearing in Fig. 12(a) mark the axial positions of the reattachment point, while those of Fig. 12(b) are located at the center of the impingement region.

Increasing κ reduces reattachment and redevelopment lengths and leads to upstream movement of peak Nu/Nu_{fd} points. For Newtonian fluids, increasing κ strengthens the corner vortex and shifts the maximum heat transfer point location from downstream to upstream of the reattachment point. For $Y = 0$ and 1, the peak Nu/Nu_{fd} values appearing downstream of the impingement region grow continuously with κ. For non-separating viscoplastic flow field or $Y = 5$, the obtained peak Nu/Nu_{fd} value is practically insensitive to variations in center-body-blockage-ratio. An examination of Figs. 8 and 12(a) and (b) reveals that all peak Nu/Nu_{fd} values appearing within the corner vortex region are proportional to the recirculation intensity. Separating viscoplastic flow fields result in finite-size, attached to the wall, impingement regions. These non-moving impingement regions are diffusion limited heat transfer zones that lead to, for $Pr > 1$, a substantial drop in wall heat transfer rates as clearly demonstrated in Fig. 12(b).

5. Concluding remarks

The impact of hydrodynamic conditions on heat transfer phenomenon in a complex viscoplastic flow field was studied by simulating non-isothermal viscoplastic flows through the geometry shown in Fig. 1. Depending on the governing parameters, suddenly expanding viscoplastic flows can display either of the following flow patterns:

- Typical separating and reattaching viscous flow field that is characterized by a recirculation zone bounded by a reattachment point (Newtonian fluids).
- A separating viscoplastic flow field that results in a weak recirculation zone bounded by a finite-size, attached to the wall, stagnant impingement region (obtained for a combination of low yield numbers and high Reynolds numbers).

- A non-separating viscoplastic flow field that forms a substantial, ramp-like, stagnant zone behind the plane of flow expansion (obtained for a combination of high yield numbers and low Reynolds numbers).

The qualitative and quantitative features of the curves that describe the axial distributions of wall heat transfer rates behind the plane of sudden expansion strongly depend on the existing flow pattern. For non-dissipative flows of $Pr > 1$ fluids, the heat transfer curves exhibit the following features:

- The first flow pattern results in a steady increase of the heat transfer rates to a peak value, around the reattachment point, followed by a continuous decline to the fully developed value obtained further downstream. The placement of an upstream solid-center-body increases the recirculation intensity and leads to a shift in the location of the peak heat transfer point from downstream to upstream of the reattachment point.
- The second flow pattern always leads to two local heat transfer peaks, one close to the corner vortex center, while the other is located downstream of the impingement region. These two peaks form due to the existence of the stagnant impingement region. Stagnant flow regions are diffusion limited heat transfer zones that substantially suppress the local heat transfer rates when $Pr > 1$.
- The third flow pattern results in a steady increase of the heat transfer rates to a peak value, downstream of the stagnant zone, followed by a continuous decline to the fully developed value. The peak heat transfer values obtained here are in general higher than those associated with the first flow pattern.

Non-dissipative flows corresponding to $Pr > 1$ substantially enhance heat transfer downstream of the expansion plane, resulted here in Nusselt numbers that were up to three times the downstream, fully developed value. Heat transfer rates behind the plane of expansion in the case of dissipative flows were lower than the fully developed values.

References

[1] R.B. Bird, G.C. Dai, B.J. Yarusso, The rheology and flow of viscoplastic materials, Rev. Chem. Eng. 1 (1) (1983) 1–70.

[2] C.R. Beverly, R.I. Tanner, Numerical analysis of three-dimensional Bingham plastic flow, J. Non-Newtonian Fluid Mech. 42 (1992) 85–115.

[3] P. Chaturani, R. Ponnalgarsamy, A study of non-Newtonian aspects of blood flow through stenosed arteries and its applications in arterial diseases, Biorheology 22 (1988) 521.

[4] R.E. Carter, R.C. Warren, Extrusion stresses, die swell, and viscous heating effects in double-base propellants, J. Rheology 31 (2) (1987) 151–173.

[5] C.-Y. Ma, J.L. White, F.C. Wiessert, K. Min, Flow patterns in carbon black filled polyethylene at the entrance to a die, J. Non-Newtonian Fluid Mech. 17 (1985) 275–287.

[6] G.C. Vradis, J. Dougher, S. Kumar, Entrance pipe flow and heat transfer for a Bingham plastic, Int. J. Heat Mass Transfer 36 (3) (1993) 543–552.

[7] T. Min, H.G. Choi, J.Y. Yoo, H. Choi, Laminar convective heat transfer of a Bingham plastic in a circular pipe—II. Numerical approach-hydrodynamically developing flow and simultaneously developing flow, Int. J. Heat Mass Transfer 40 (15) (1997) 3689–3701.

[8] G.C. Vradis, K.J. Hammad, Heat transfer in flows of non-Newtonian Bingham fluids through axisymmetric sudden expansions and contractions, Numerical Heat Transfer (A) 28 (3) (1995) 339–355.

[9] K.J. Hammad, G.C. Vradis, Creeping flow of a Bingham plastic through axisymmetric sudden contractions with viscous dissipation, Int. J. Heat Mass Transfer 39 (8) (1996) 1555–1568.

[10] K.J. Hammad, F. Wang, M.V. Ötügen, G.C. Vradis, Suddenly expanding axisymmetric flow of a yield stress fluid, Album of Visualization 14 (1997).

[11] E.O. Macagno, T. Hung, Computational and experimental study of a captive annular eddy, J. Fluid Mech. 28 (1967) 43–63.

[12] J.W. Baughn, M.A. Hoffman, R.K. Takahashi, D. Lee, Heat transfer downstream of an abrupt expansion in the transition Reynolds number regime, J. Heat Transfer 109 (1987) 37–42.

[13] B. Pak, Y.I. Cho, S.U.S. Choi, Separation and reattachment of non-Newtonian fluid flows in a sudden expansion pipe, J. Non-Newtonian Fluid Mech. 37 (2-3) (1990) 175.

[14] D. Badekas, D.D. Knight, Eddy correlations for laminar axisymmetric sudden expansion flows, J. Fluids Eng. 114 (1992) 119–121.

[15] T.A. Myrum, S. Thumma, Freezing of a paraffin flow downstream of an abrupt expansion, Int. J. Heat Mass Transfer 35 (2) (1992) 421–432.

[16] G.C. Vradis, K.J. Hammad, Strongly coupled block-implicit solution technique for non-Newtonian convective heat transfer problems, Numerical Heat Transfer (B) 33 (1998) 79–97.

[17] P.J. Oliveira, F.T. Pinho, A. Schulte, A general correlation for the local loss coefficient in Newtonian axisymmetric sudden expansions, Int. J. Heat Fluid Flow 19 (6) (1998) 655–660.

[18] K.J. Hammad, M.V. Ötügen, E.B. Arik, A PIV study of the laminar axisymmetric sudden expansion flow, Exp. Fluids 26 (1999) 266–272.

[19] I.A. Feurstein, G.K. Pike, G.F. Rounds, Flow in an abrupt expansion as a model for biological mass transfer experiments, J. Biomech. 8 (1975) 41–51.

[20] E.J. Roschke, L.H. Back, The influence of upstream flow conditions on flow reattachment lengths downstream of an abrupt circular channel expansion, J. Biomech. 9 (1976) 481–483.

[21] A. Pollard, A contribution on the effects of inlet conditions when modeling stenosis using sudden expansions, J. Biomech. 14 (1981) 349–355.
[22] P. Ma, X. Li, D.N. Ku, Heat and mass transfer in a separated flow region for high Prandtl and Schmidt numbers under pulsatile conditions, Int. J. Heat Mass Transfer 37 (17) (1994) 2723–2736.
[23] G.A. Trusky, K.M. Barber, T.C. Robey, L.A. Olivier, M.P. Combs, Characterization of a sudden expansion flow chamber to study the response of endothelium to flow recirculation, J. Biomech. Eng. 117 (2) (1995) 203–210.
[24] T.C. Papanastasiou, Flow of materials with yield, J. Rheology 31 (5) (1987) 385–403.
[25] K.R.J. Ellwood, G.C. Georgiou, T.C. Papanastasiou, J.O. Wilkes, Laminar jets of Bingham plastic liquids, J. Rheology 34 (1990) 787–812.
[26] K.J. Hammad, Experimental and computational study of laminar axisymmetric recirculating flows of Newtonian and non-Newtonian fluids. Ph.D. Dissertation, Mechanical, Aerospace and Manufacturing Engineering Department, Polytechnic University, Brooklyn, NY, 1997.
[27] P.S. Scott, F. Mirza, Finite-element simulation of laminar viscoplastic flows with regions of recirculation, J. Rheology 32 (4) (1988) 387–400.
[28] G.C. Vradis, M.V. Ötügen, The axisymmetric sudden expansion flow of a non-Newtonian viscoplastic fluid, J. Fluids Eng. 119 (1997) 193–200.
[29] K.J. Hammad, M.V. Ötügen, G.C. Vradis, E.B. Arik, Laminar flow of a nonlinear viscoplastic fluid through an axisymmetric sudden expansion, J. Fluids Eng. 121(2) (1999) 488–496.
[30] P. Payvar, Asymptotic Nusselt numbers for dissipative non-Newtonian flow through ducts, Appl. Sci. Res. 27 (1973) 297–306.